Fimsbactin and Acinetobactin Compete for the Periplasmic Siderophore Binding Protein BauB in Pathogenic *Acinetobacter baumannii*

Tabbetha J. Bohac, Luting Fang, Daryl E. Giblin, and Timothy A. Wencewicz*

Department of Chemistry, Washington University in St. Louis, One Brookings Drive, St. Louis, MO, 63130, USA

*Correspondence to TAW:

Email: wencewicz@wustl.edu

Ph: 314-935-7247

Fax: 314-935-4481

ORCID: 0000-0002-5839-6672

Table of Contents

I. Supplementary Figures

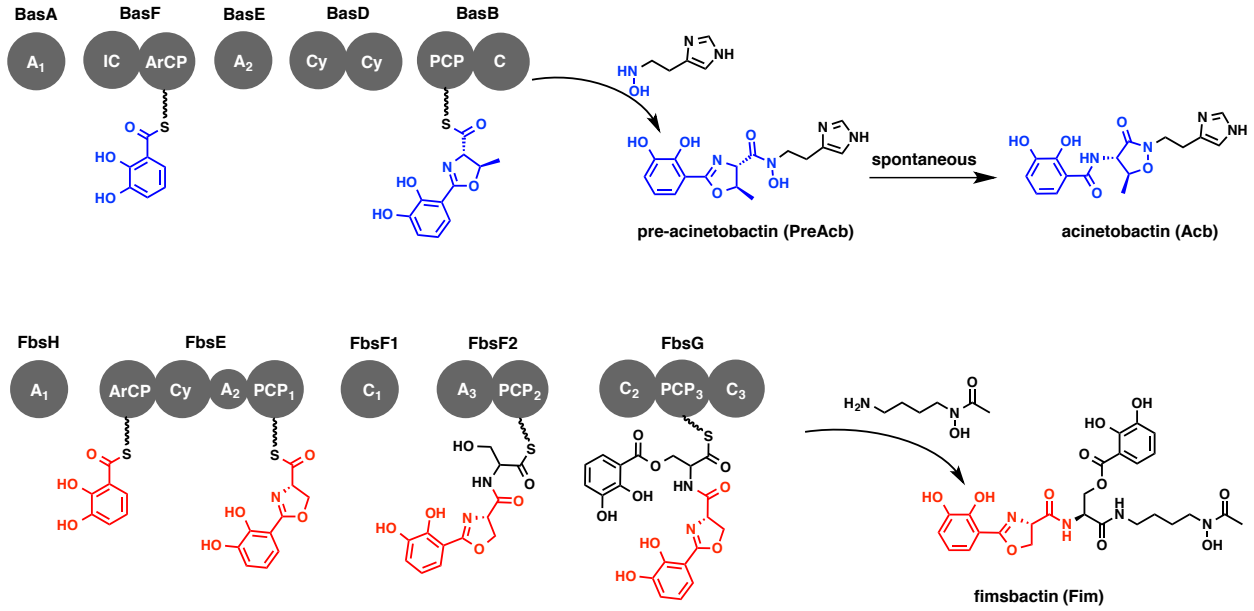

Supplementary Figure 1. Predicted biosynthesis of acinetobactin and fimsbactin in *A. baumannii* ATCC 17978.[1, 2] Non-ribosomal peptide synthetase (NRPS) assembly lines for acinetobactin (top) and fimsbactin A (bottom) share a common precursor, 2,3-DHB, and a common phenolate oxazoline motif. Pre-acinetobactin (PreAcb) is the kinetic product released from the NRPS assembly line. PreAcb undergoes spontaneous isomerization to the thermodynamic product acinetobactin (Acb).

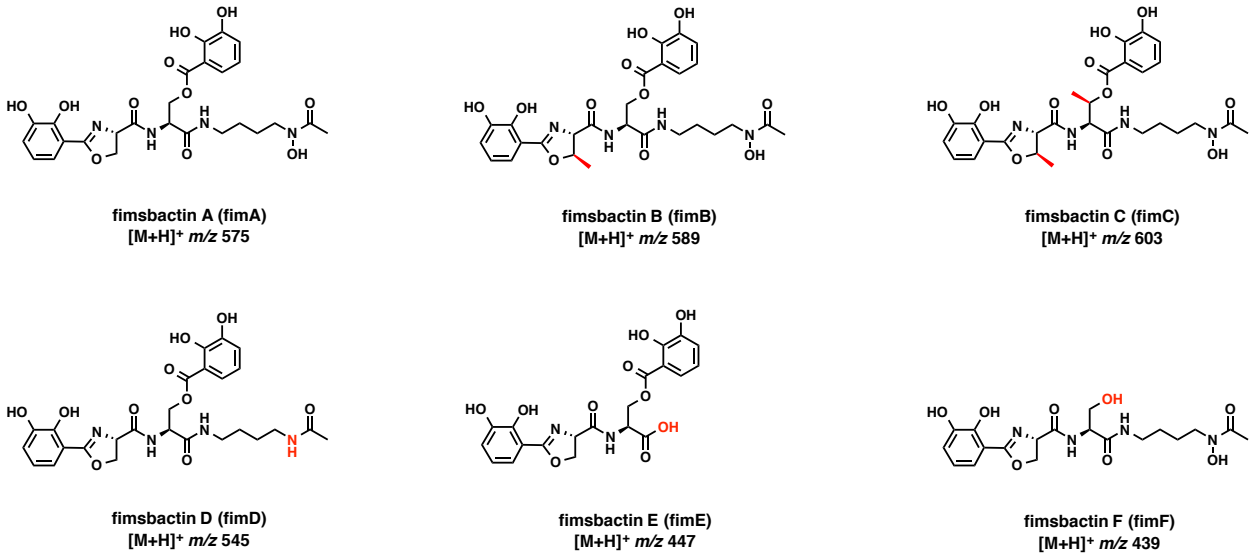

Supplementary Figure 2. Structures and *m/z* values for $[M+H]^+$ molecular ions of fimsbactin A–F.[1] Structural differences are highlighted in red.

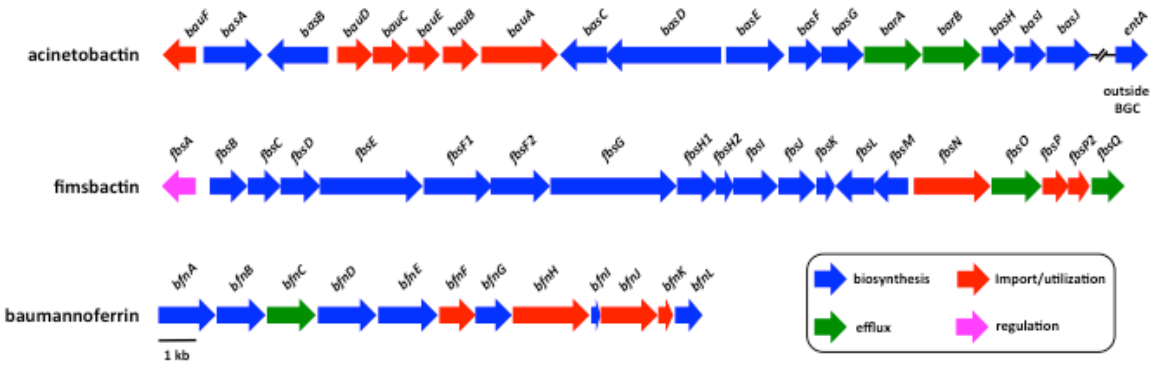

Supplementary Figure 3. Biosynthetic gene clusters for acinetobactin[2], fimsbactin[1], and baumannoferrin[3] from *A. baumannii* ATCC 17978 along with annotated genes.

Fimsbactin Biosynthetic Gene Clusters

AbPK1 (GenBank: GCA_002753915.1)

AB042 (GenBank: GCA_001941765.1)

D36 (GenBank: GCA_001399655.1)

Strain ATCC 17978 (GenBank: GCA_001593425)

ATCC 17978-mmf (GenBank: GCA_001077675.1)

Acinetobactin Biosynthetic Gene Clusters

AbPK1 (GenBank: GCA_002753915.1)

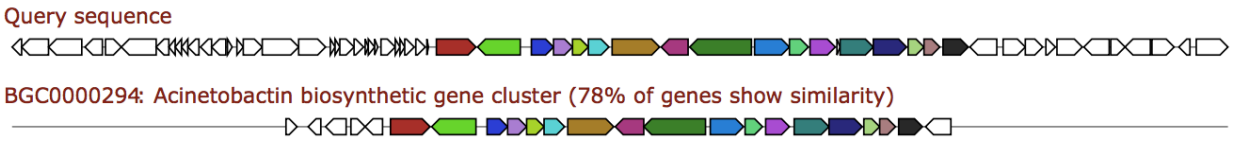

AB042 (GenBank: GCA_001941765.1)

D36 (GenBank: GCA_001399655.1)

Strain ATCC 17978 (GenBank: GCA_001593425)

ATCC 17978-mmf (GenBank: GCA_001077675.1)

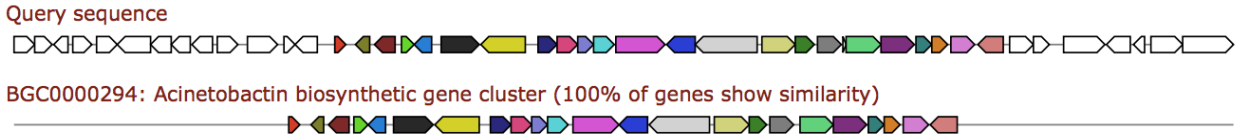

Acinetoferrin/Baumannoferrin Biosynthetic Gene Clusters

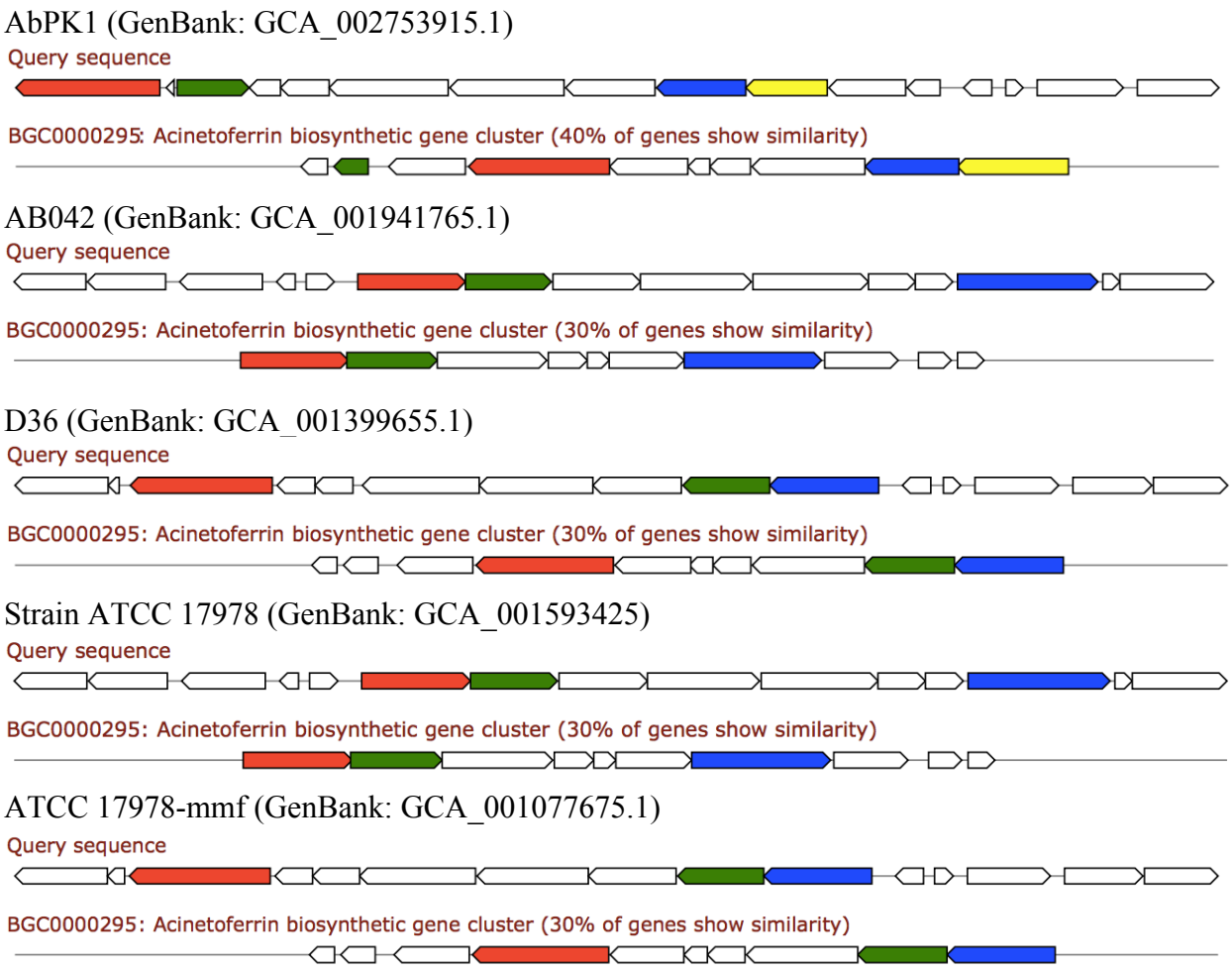

Supplementary Figure 4. AntiSMASH[4] analysis of putative fimsbactin *A. baumannii* producers identified from BLASTp analysis of *A. baumannii* genomes reveals conservation of acinetobactin and baumannoferrin biosynthetic gene clusters (BGCs). The acinetoferrin BGC is the reference in the antiSMASH database. Acinetoferrin and baumannoferrin BGCs share homology, so comparison for all strains was made to the acinetoferrin BGC.[5]

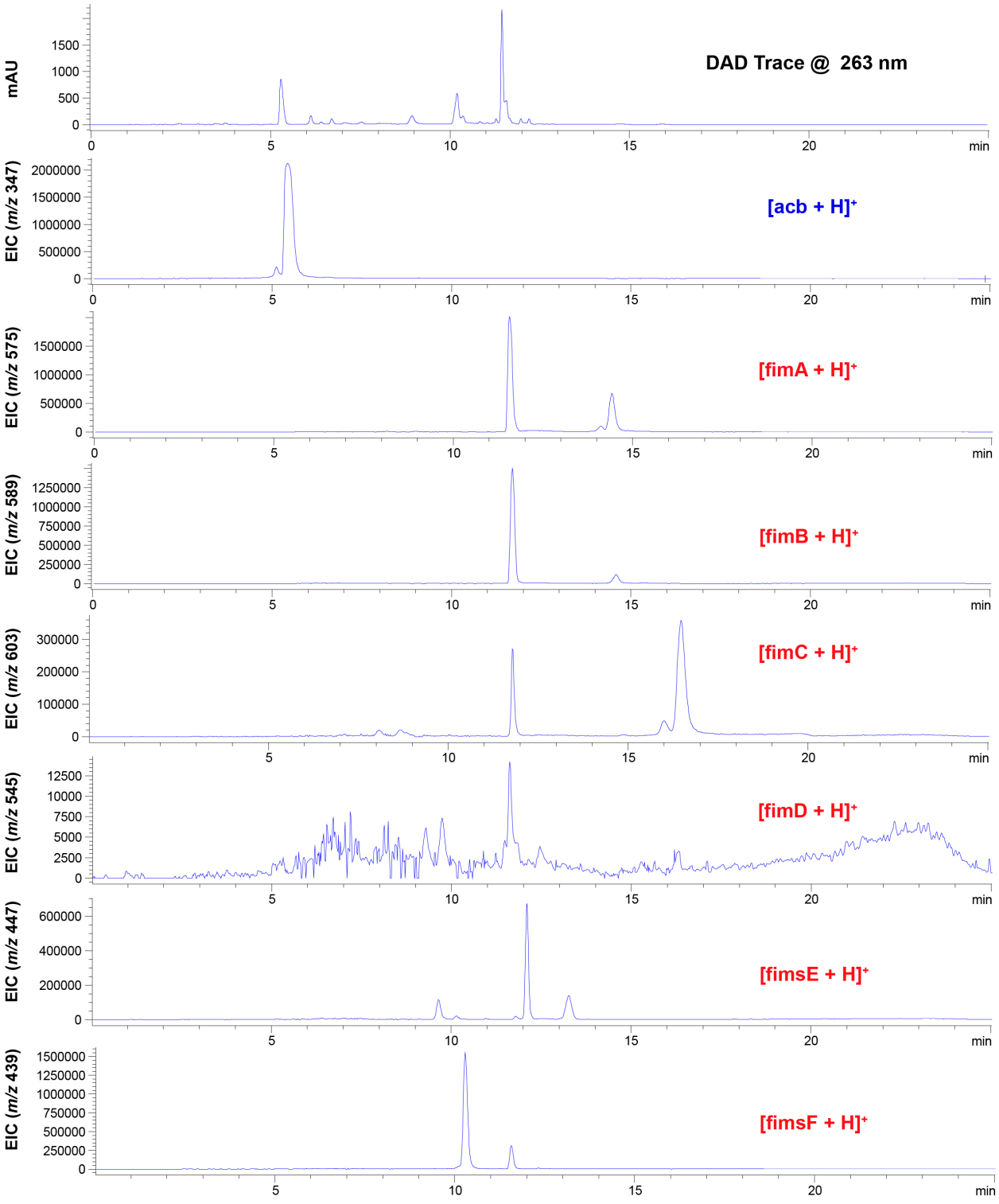

Supplementary Figure 5. Diode array optical absorbance detection (DAD) and extracted ion chromatograms (EICs) for fimsbactin A–F $[M+H]^+$ ions from LCMS analysis of *A. baumannii* ATCC 17978 culture supernatant extractions (**Trial #1**) using ESI ionization in positive ion mode. The x-axis represents retention time (min) for all chromatograms.

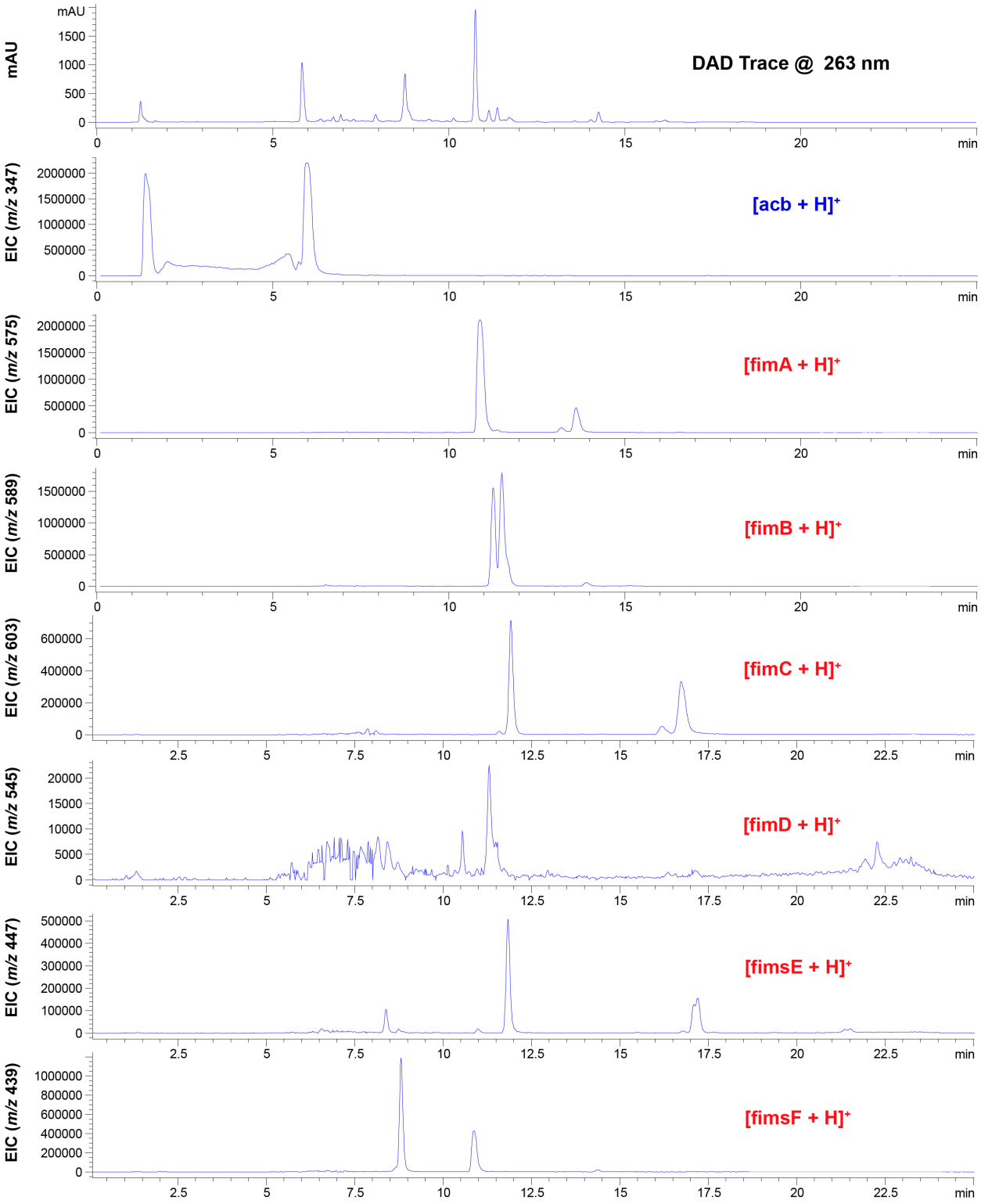

Supplementary Figure 6. Diode array optical absorbance detection (DAD) and extracted ion chromatograms (EICs) for fimsbactin A–F $[M+H]^+$ ions from LCMS analysis of *A. baumannii* ATCC 17978 culture supernatant extractions (**Trial #2**) using ESI ionization in positive ion mode. The x-axis represents retention time (min) for all chromatograms.

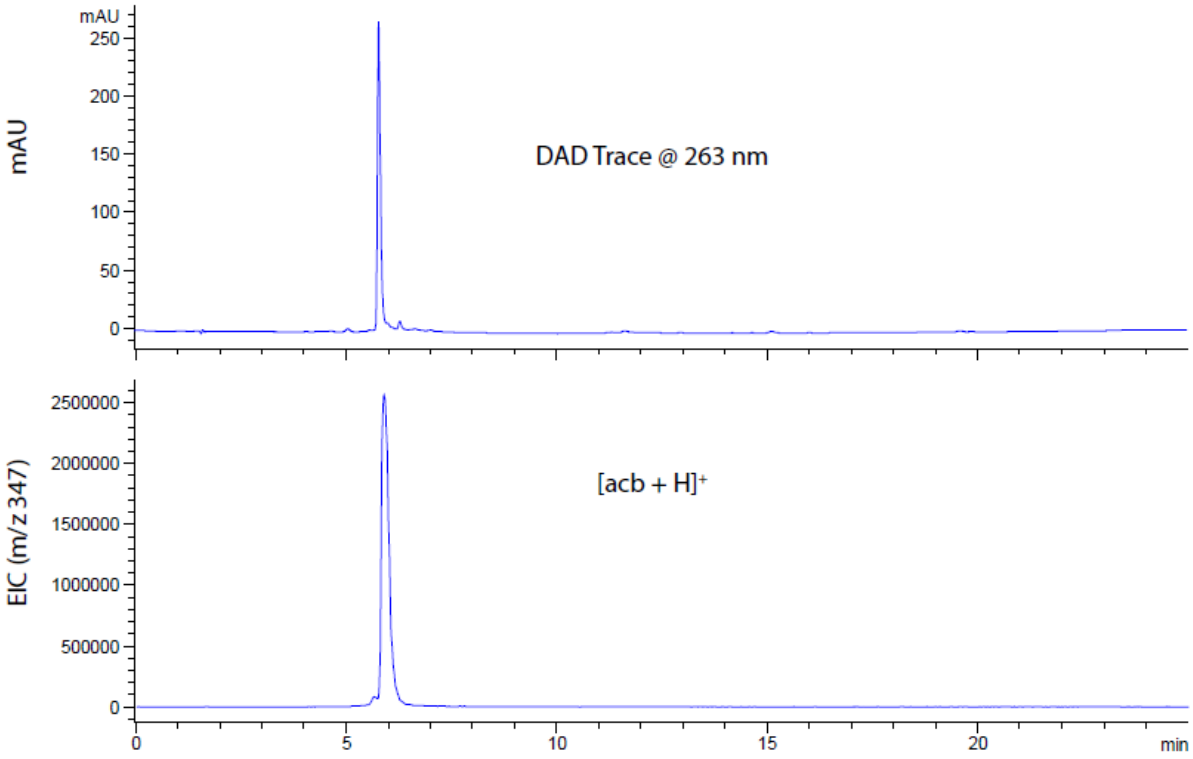

Supplementary Figure 7. Diode array optical absorbance detection (DAD) and extracted ion chromatograms (EICs) for Acb $[M+H]^+$ ions from LCMS analysis of HPLC-purified Acb from *A. baumannii* ATCC 17978 using ESI ionization in positive ion mode. The x-axis represents retention time (min) for all chromatograms.

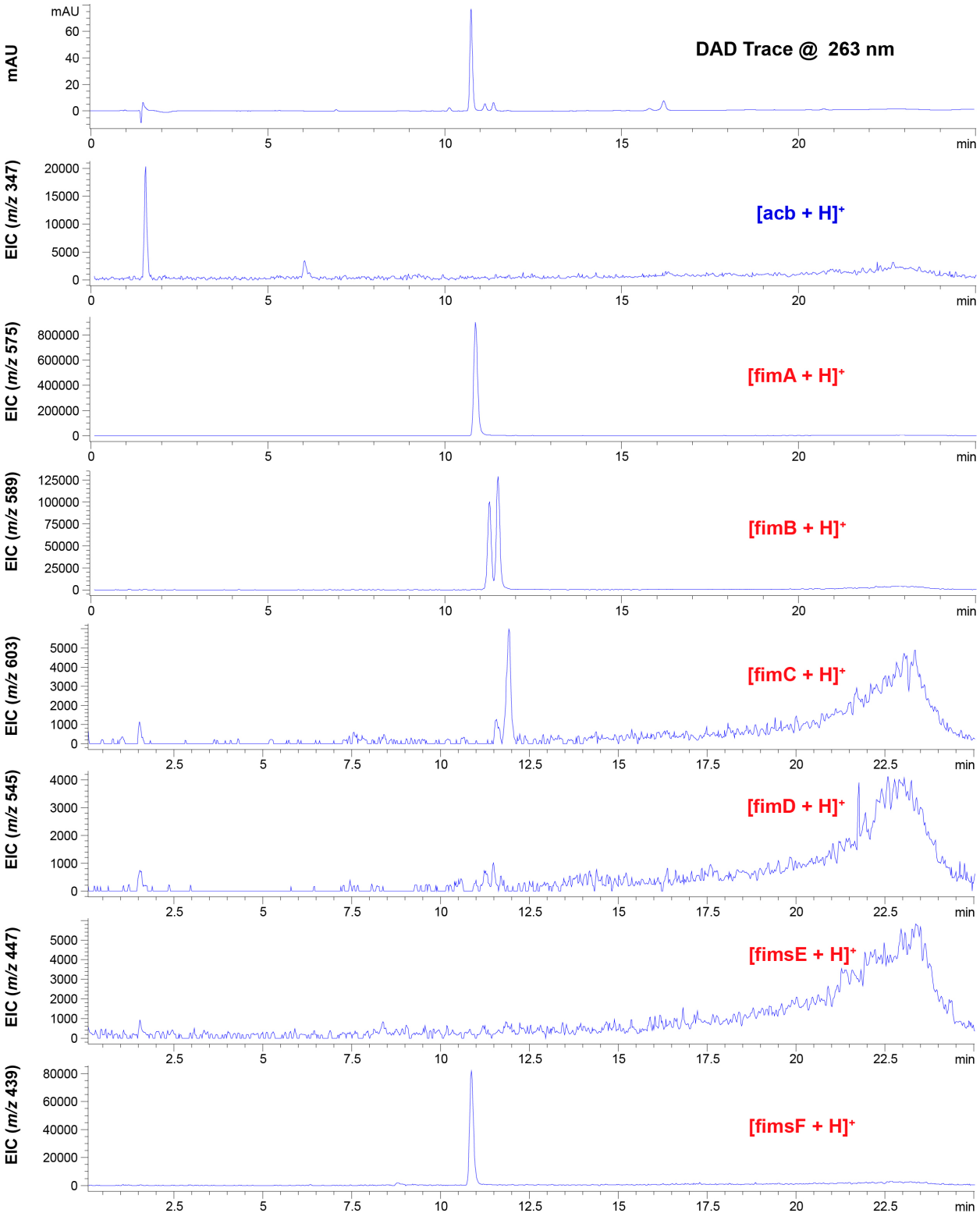

Supplementary Figure 8. Diode array optical absorbance detection (DAD) and extracted ion chromatograms (EICs) for fimsbactin A–F $[M+H]^+$ ions from LCMS analysis of HPLC-purified fimsbactin A from *A. baumannii* ATCC 17978 (**Trial #1**) using ESI ionization in positive ion mode. The x-axis represents retention time (min) for all chromatograms.

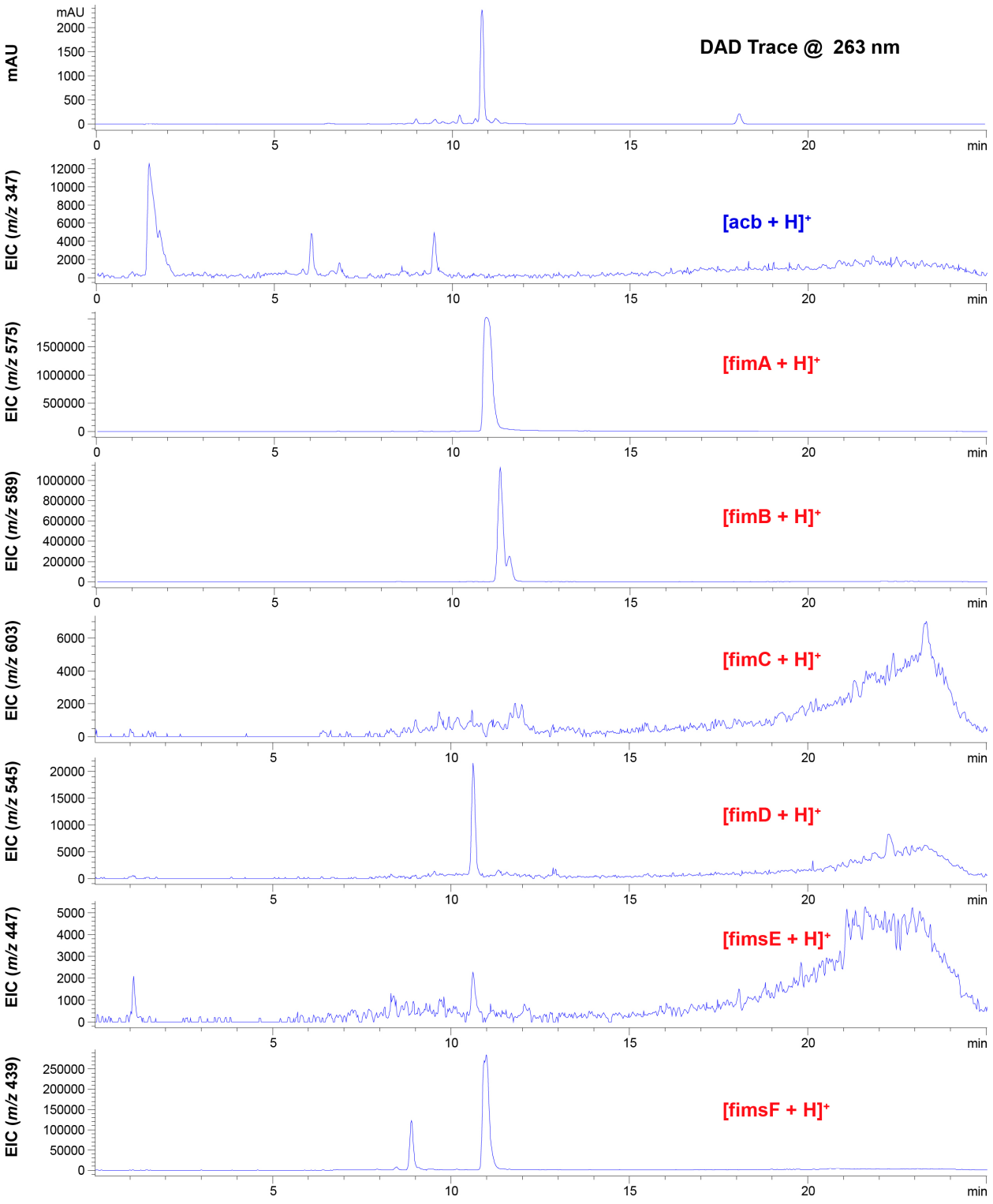

Supplementary Figure 9. Diode array optical absorbance detection (DAD) and extracted ion chromatograms (EICs) for fimsbactin A–F $[M+H]^+$ ions from LCMS analysis of HPLC-purified fimsbactin A from *A. baumannii* ATCC 17978 (**Trial #2**) using ESI ionization in positive ion mode. The x-axis represents retention time (min) for all chromatograms.

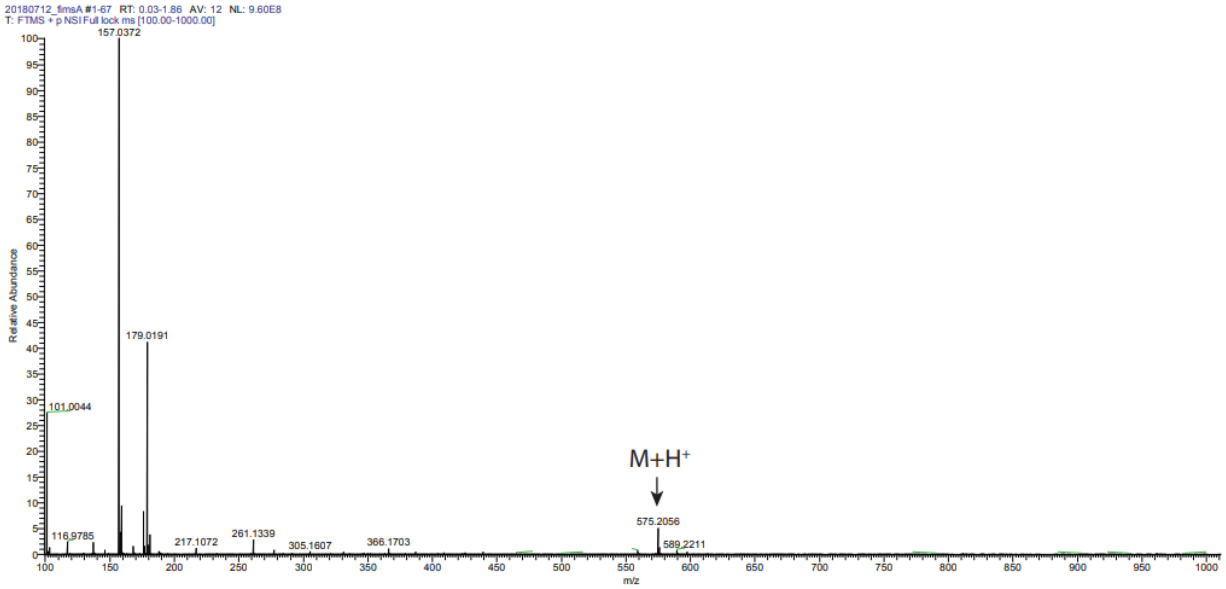

Supplemental Figure 10. High-resolution ESI MS (positive ion mode) of fimsbactin A purified by prep-HPLC from *A. baumannii* ATCC 17978 culture supernatant (**Trial #1**). Expected $[M+H]^+$ for $C_{26}H_{31}N_4O_{11}$ 575.1984, found 575.2056.

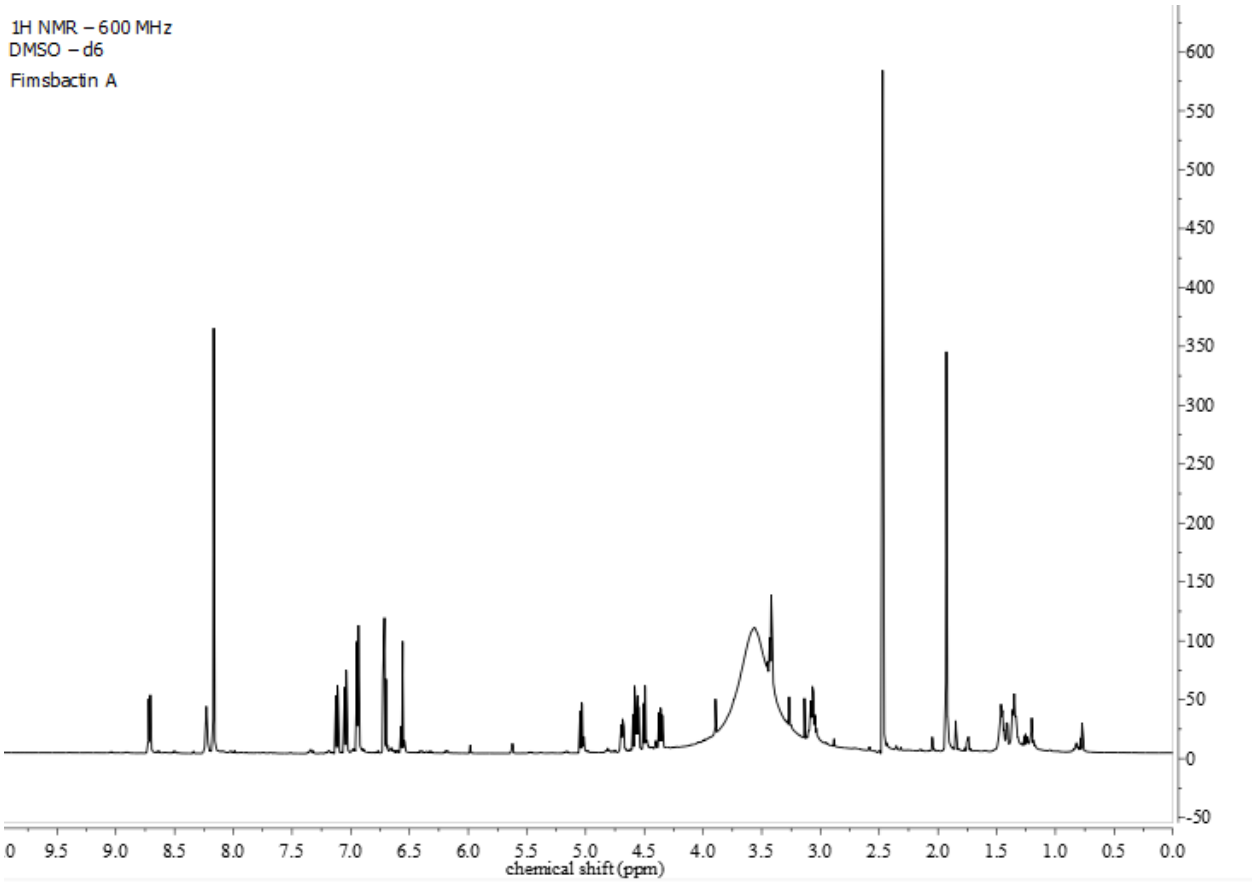

Supplemental Figure 11. ^{1}H-NMR (600 MHz, DMSO-*d6*) spectrum of purified fimsbactin A purified by prep-HPLC from *A. baumannii* ATCC 17978. The x-axis is chemical shift given in parts per million (ppm). The y-axis is arbitrary peak intensity.

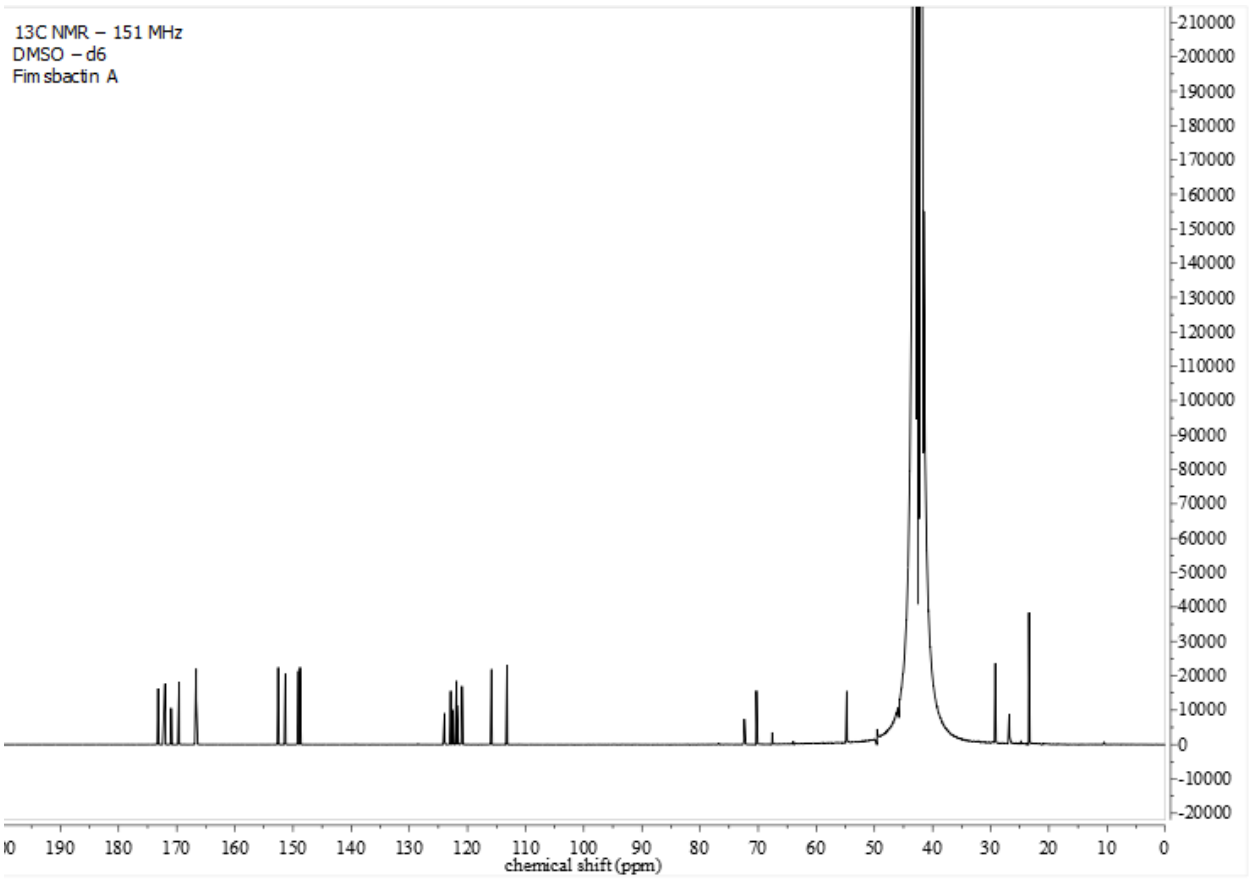

Supplemental Figure 12. ^{13}C-NMR (151 MHz, DMSO-*d6*) spectrum of purified fimsbactin A purified by prep-HPLC from *A. baumannii* ATCC 17978. The x-axis is chemical shift given in parts per million (ppm). The y-axis is arbitrary peak intensity.

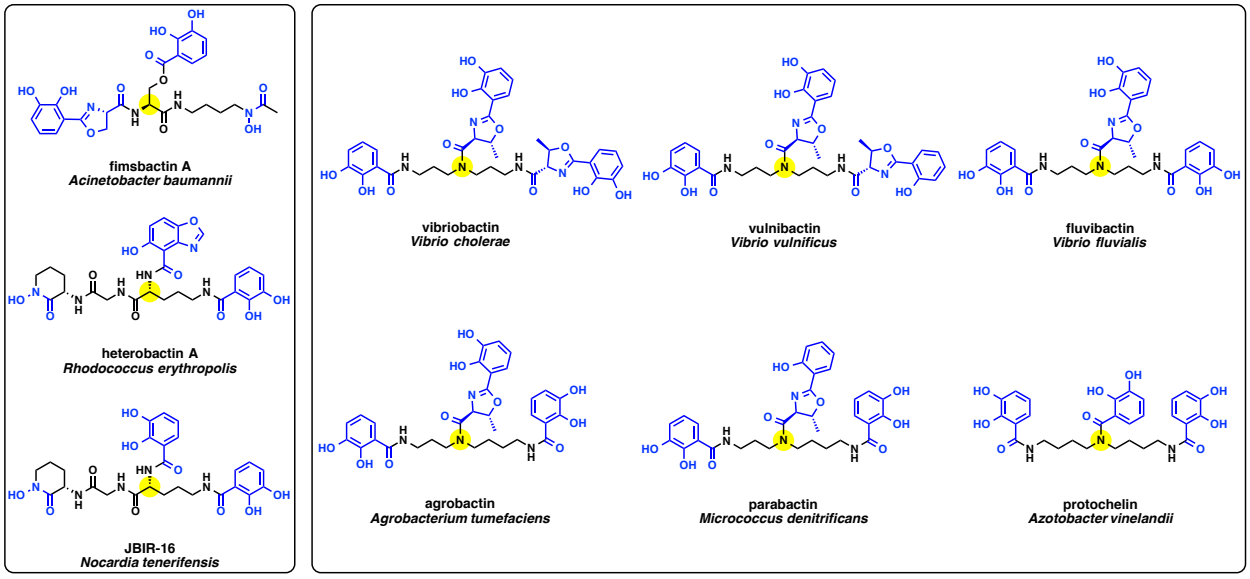

Supplementary Figure 13. Structures and microbial producers of amino acid-based siderophores fimsbactin A[1], heterobactin A[6], and JBIR-16[7], and spermidine-based siderophores vibriobactin[8], vulnibactin[9], fluvibactin[10], agrobactin[11], parabactin[12], and protochelin[13]. Iron chelating groups are shown in blue. The tetrehdral branch point for metal chelating ligands is highlighted by a yellow circle.

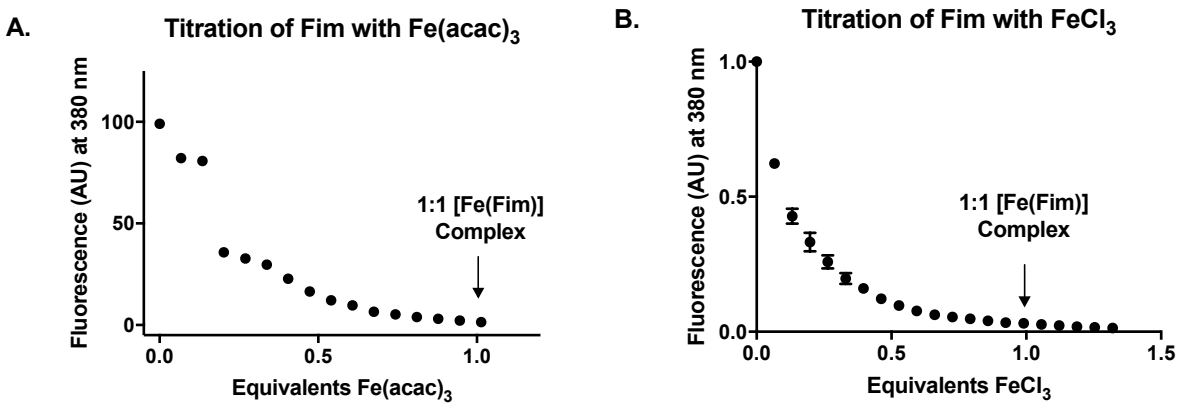

Supplementary Figure 14. Titration of Fim with (**A**) $Fe(acac)_3$ and (**B**) $FeCl_3$ in methanol. Graphs depict fluorescence ($\lambda_{excitation}$ = 330 nm; $\lambda_{emission}$ = 380 nm) vs equivalents of ferric iron source showing a titration end point correlating with a 1:1 final stoichiometry for the [Fe(Fim)] ferric complex. Titration with $FeCl_3$ was performed as two independent trials. Error bars represent standard deviation from the mean.

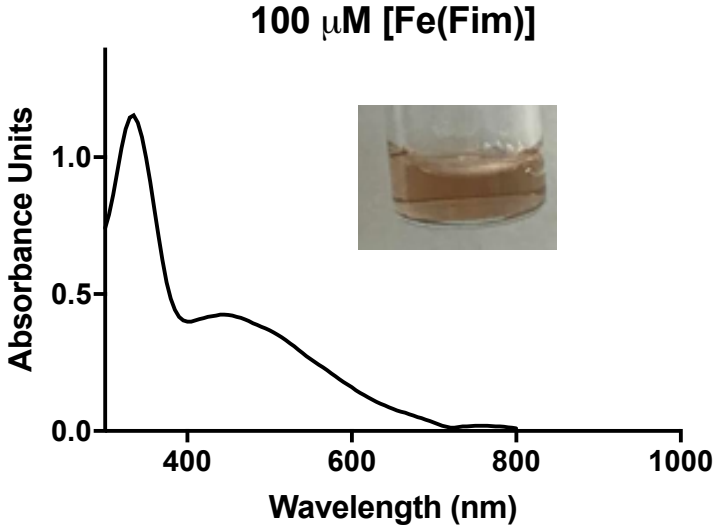

Supplementary Figure 15. Optical absorbance spectrum of the *holo*-[Fe(Fim)] complex at 100 μM in phosphate buffer (50 mM potassium phosphate pH 8.0, 150 mM NaCl, 1 mM DTT, 5% glycerol). The molar exctinction coefficient (ε) of *holo*-[Fe(Fim)] was determined to be 4255 M^{-1} cm^{-1} at 445 nm. The inset shows the visible color of the [Fe(Fim)] solution at 100 μM.

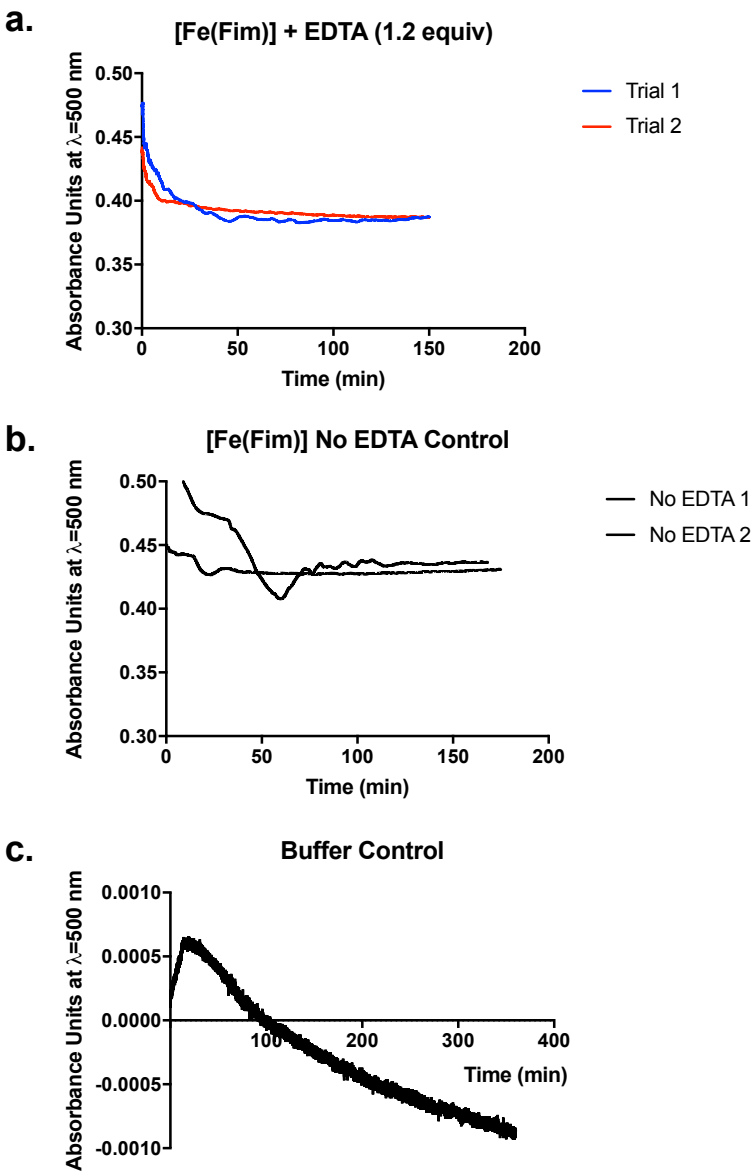

Supplementary Figure 16. Decay plots for EDTA competition assays with [Fe(Fim)]. Graphs depict absorbance at 500 nm (y-axis) vs time (x-axis) for (**A**) EDTA (1.2 equiv) plus [Fe(Fim)], (**B**) [Fe(Fim)], and (**C**) buffer only. Each experiment was performed in duplicate as independent trials. The apparent K_{Fe} for [Fe(Fim)] was calculated using the final absorbance values after 150 minutes according to equations (1)–(11) shown on page S32. The final absorbance values at 500 nm were 0.3873 (trial #1 w/ EDTA), 0.3870 (trial #2 w/ EDTA), 0.4292 (trial #1 w/o EDTA), and 0.4357 (trial #2 w/o EDTA).

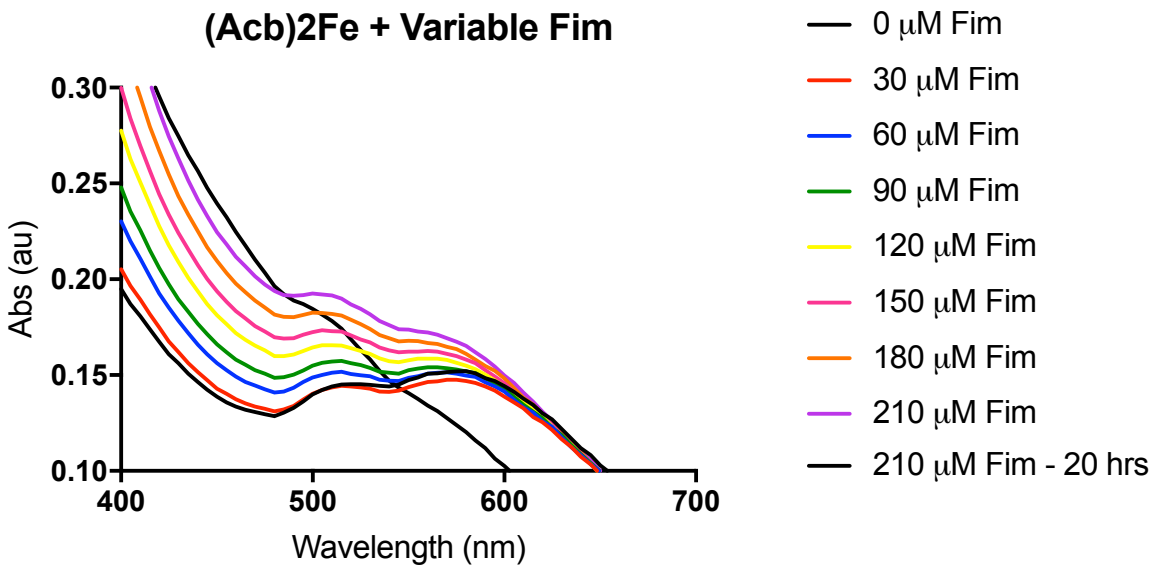

Supplementary Figure 17. Titration of 100 μM [$Fe(Acb)_2$] with Fim reveals slow exchange of iron leading to complete formation of [Fe(Fim)]. Optical absorbance spectra were collected for each concentration after 20 min in phosphate buffer (50 mM potassium phosphate pH 8.0, 150 mM NaCl, 1 mM DTT, 5% glycerol). The final optical absorbance spectrum with 210 μM *apo*-Fim added was measured after 20 hours.

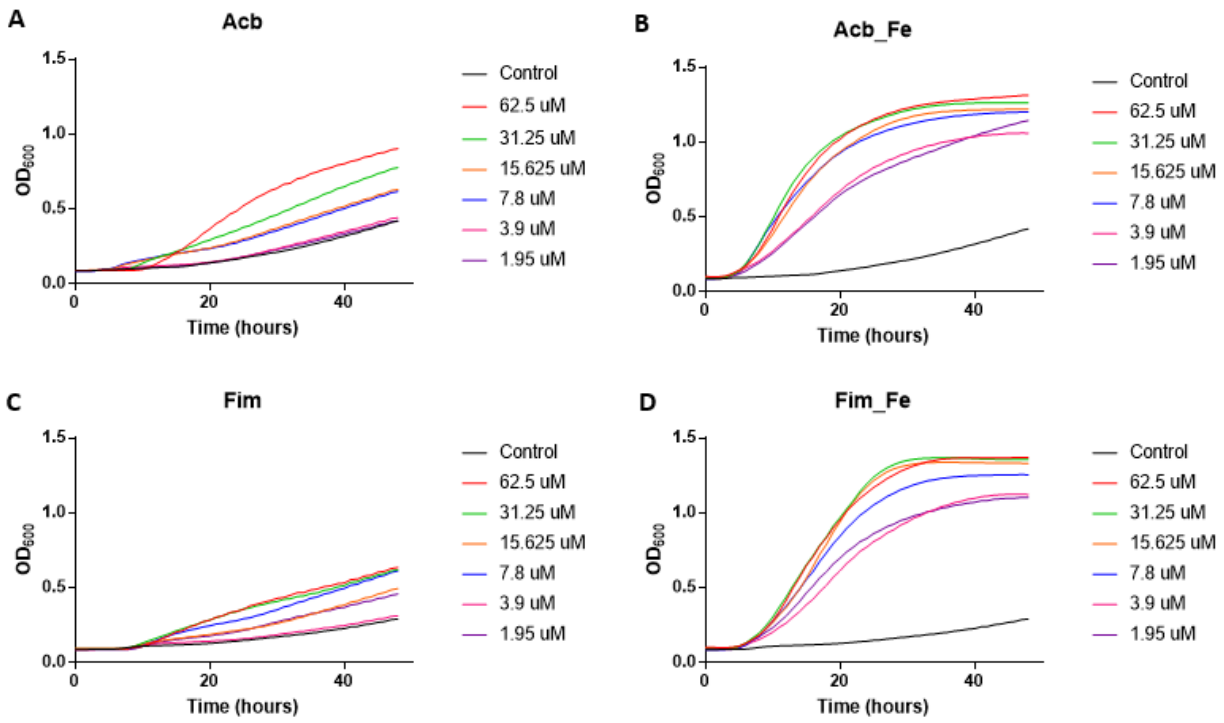

Supplementary Figure 18. Dose dependent growth promotion of *A. baumannii* ATCC 17978 by (A) *apo*-acinetobactin (Acb), (B) *holo*-acinetobactin (Acb_Fe), (C) *apo*-fimsbactin (Fim), and (D) *holo*-fimsbactin (Fim_Fe). Line graphs depict the growth of *A. baumannii* ATCC 17978 in M9 minimal medium supplemented with 175 μM 2,2′-dipyridyl (DIP) determined by measuring the optical density at 600 nm (OD_{600}) as a function of time in the presence of variable siderophore concentrations. All experiments were performed in triplicate. Error bars are shown in **Supplementary Figure 19**. Data from these plots were used to create the line and bar graphs shown in **Figure 3** in the main text.

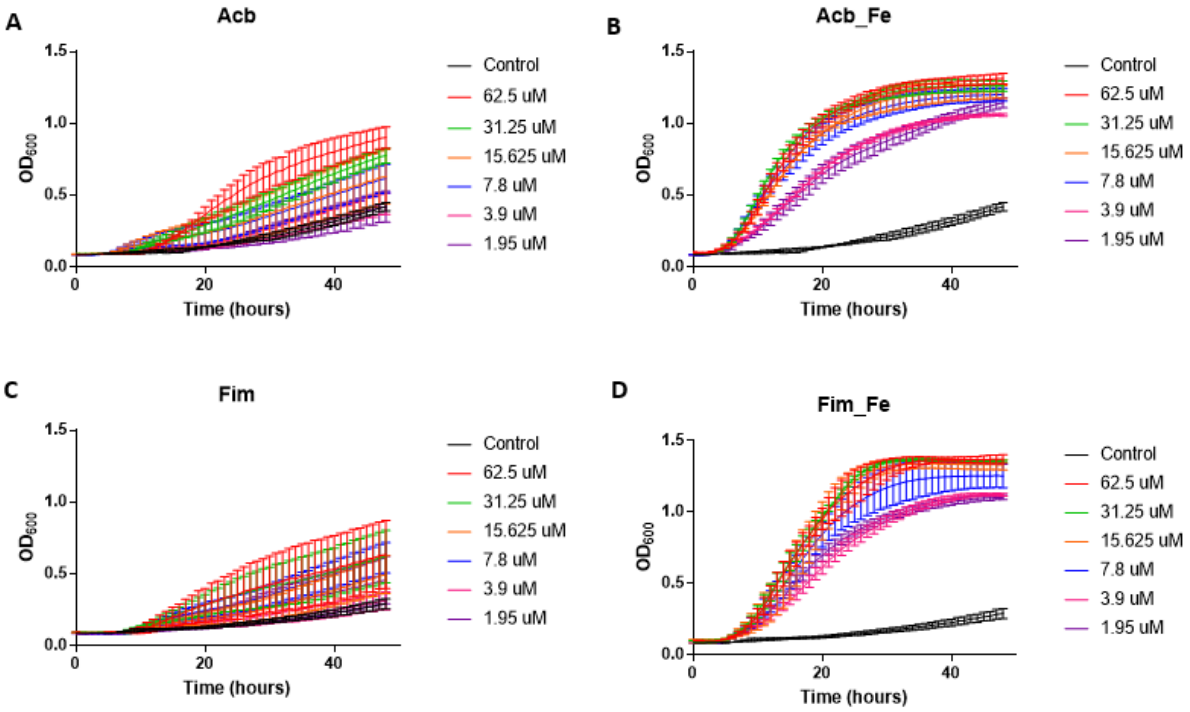

Supplementary Figure 19. Dose dependent growth promotion of *A. baumannii* ATCC 17978 by (A) *apo*-acinetobactin (Acb), (B) *holo*-acinetobactin (Acb_Fe), (C) *apo*-fimsbactin (Fim), and (D) *holo*-fimsbactin (Fim_Fe). Line graphs depict the growth of *A. baumannii* ATCC 17978 in M9 minimal medium supplemented with 175 μM 2,2′-dipyridyl (DIP) determined by measuring the optical density at 600 nm (OD_{600}) as a function of time in the presence of variable siderophore concentrations. Error bars represent standard deviations from the mean for three independent trials. Line graphs are shown without error bars for clarity in **Supplementary Figure 18**. Data from these plots were used to create the line and bar graphs shown in **Figure 3** in the main text.

A. Acinetobactin + Fimsbactin A

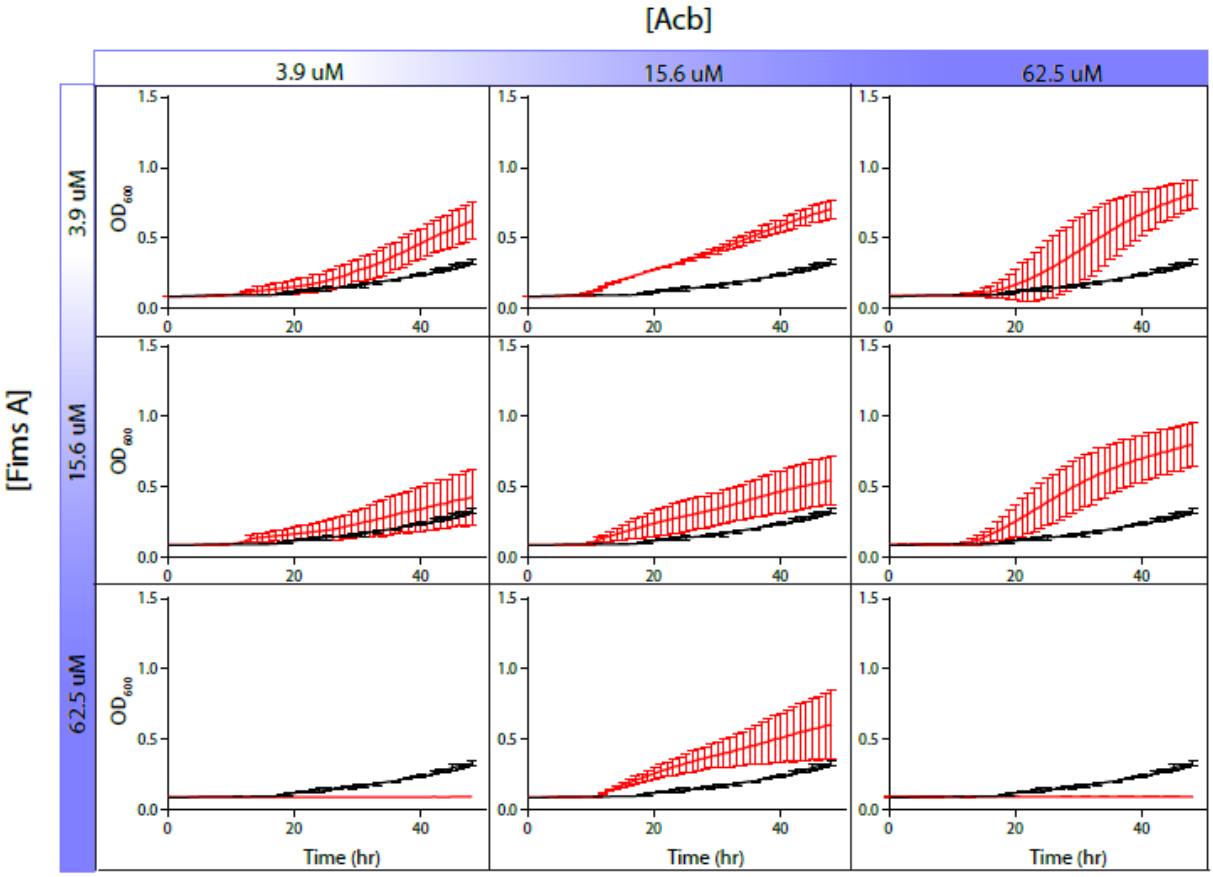

B. Acinetobactin + Fimsbactin A - Fe

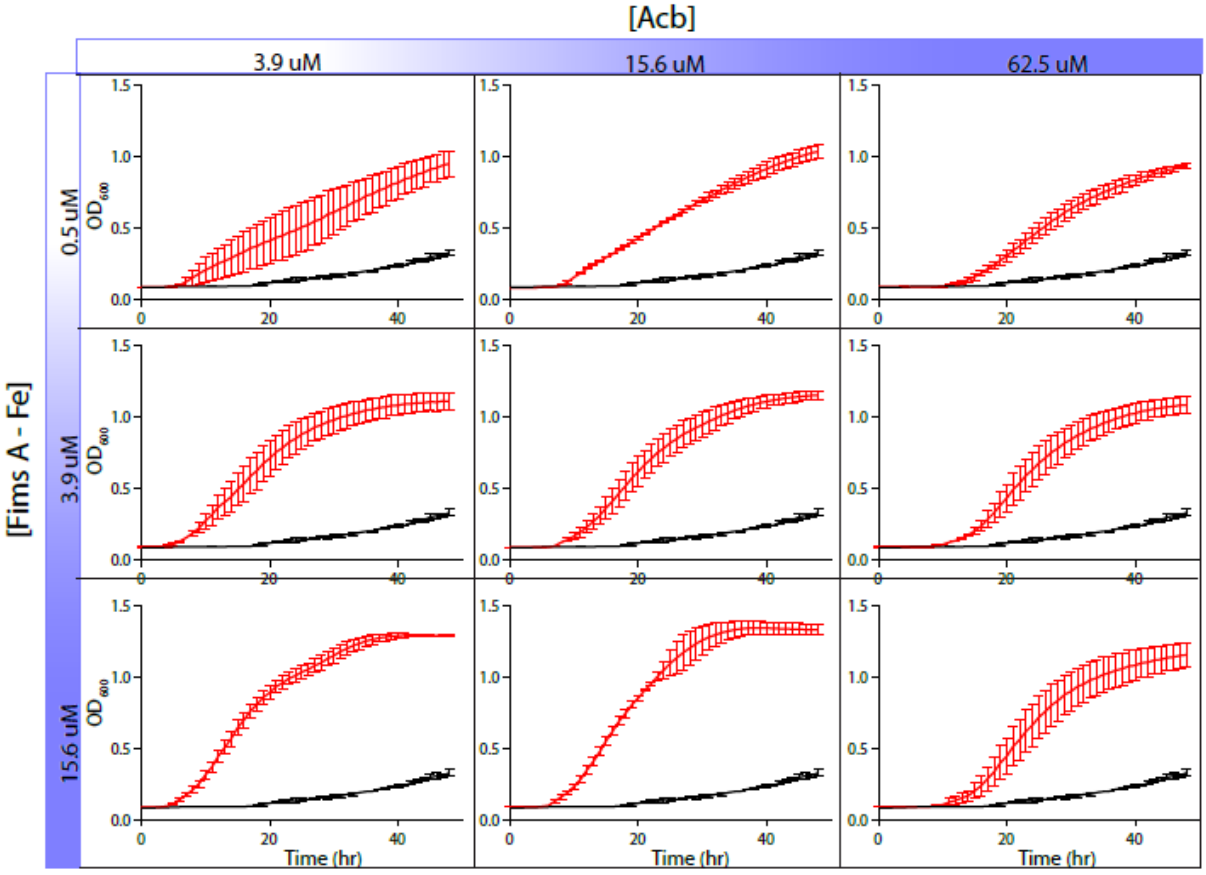

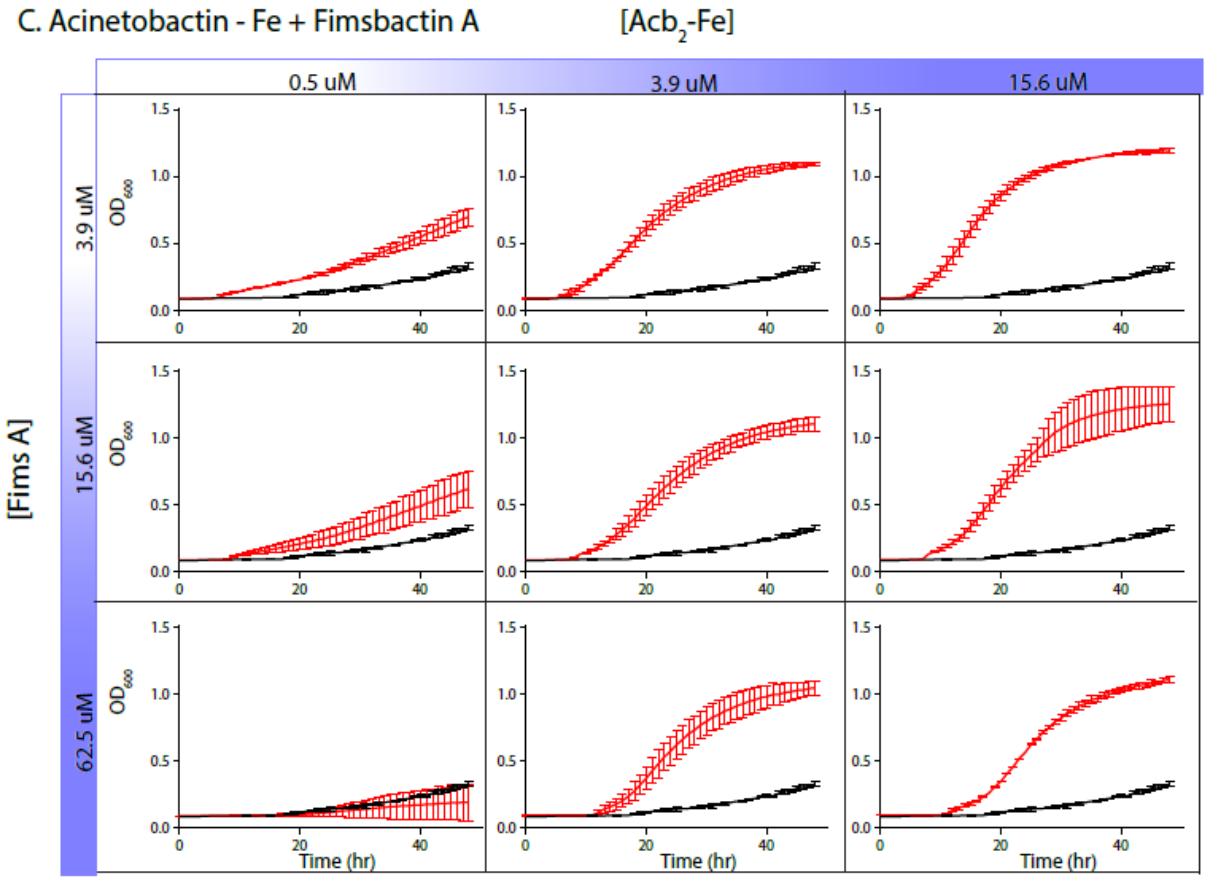
C. Acinetobactin - Fe + Fimsbactin A
[Acb2-Fe]
0.5 uM
3.9 uM
15.6 uM
[Fims A]
3.9 uM
15.6 uM
62.5 uM
OD600
Time (hr)

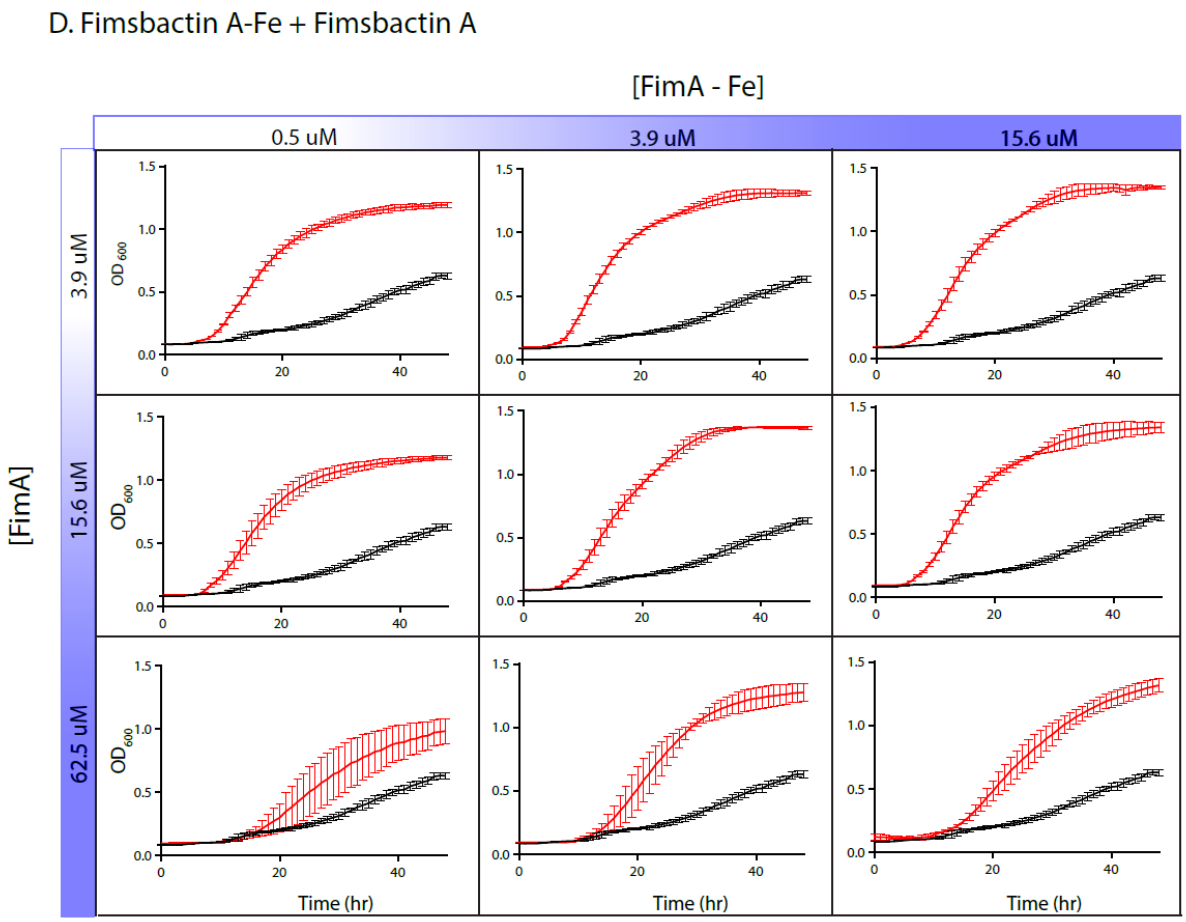

Supplementary Figure 20. Influence of *apo*- and *holo*-siderophore combinations on the growth of *A. baumannii* ATCC 17978. Line graphs depict the growth of *A. baumannii* ATCC 17978 in M9 minimal medium supplemented with 175 μM 2,2′-dipyridyl (DIP) determined by measuring the optical density at 600 nm (OD_{600}) as a function of time in the presence of variable concentrations of siderophore mixtures. For all graphs, siderophore concentration gradients are provide on the x-axis and y-axis of the checkerboard. The black line graph represents bacterial growth without addition of siderophores. The red line graph represents bacterial growth in the presence of variable concentrations of (A) *apo*-Fim and *apo*-Acb, (B) *holo*-FimFe and *apo*-Acb, (C) *apo*-Fim and *holo*-Acb_2Fe, or (D) *apo*-Fim and *holo*-FimFe. Error bars represent standard deviations from the mean for two independent trials. Data from these plots were used to create bar graphs shown in **Figure 4** in the main text.

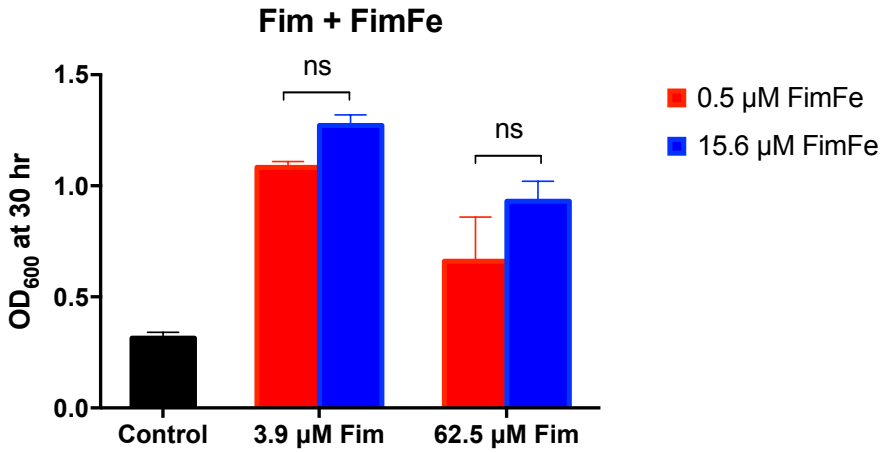

Supplementary Figure 21. Influence of *apo*-Fim *holo*-FimFe combinations on *A. baumannii* growth. Bar graphs depict the comparison of *A. baumannii* ATCC 17978 growth measured by optical density at 600 nm (OD_{600}) values after 30 hours at 37 °C in the presence of variable concentrations of (**a**) Fim and Acb, (**b**) Fim and Acb_2Fe, and (**c**) FimFe and Acb. Error bars represent standard deviations from the mean for two independent trials. ns = not significant

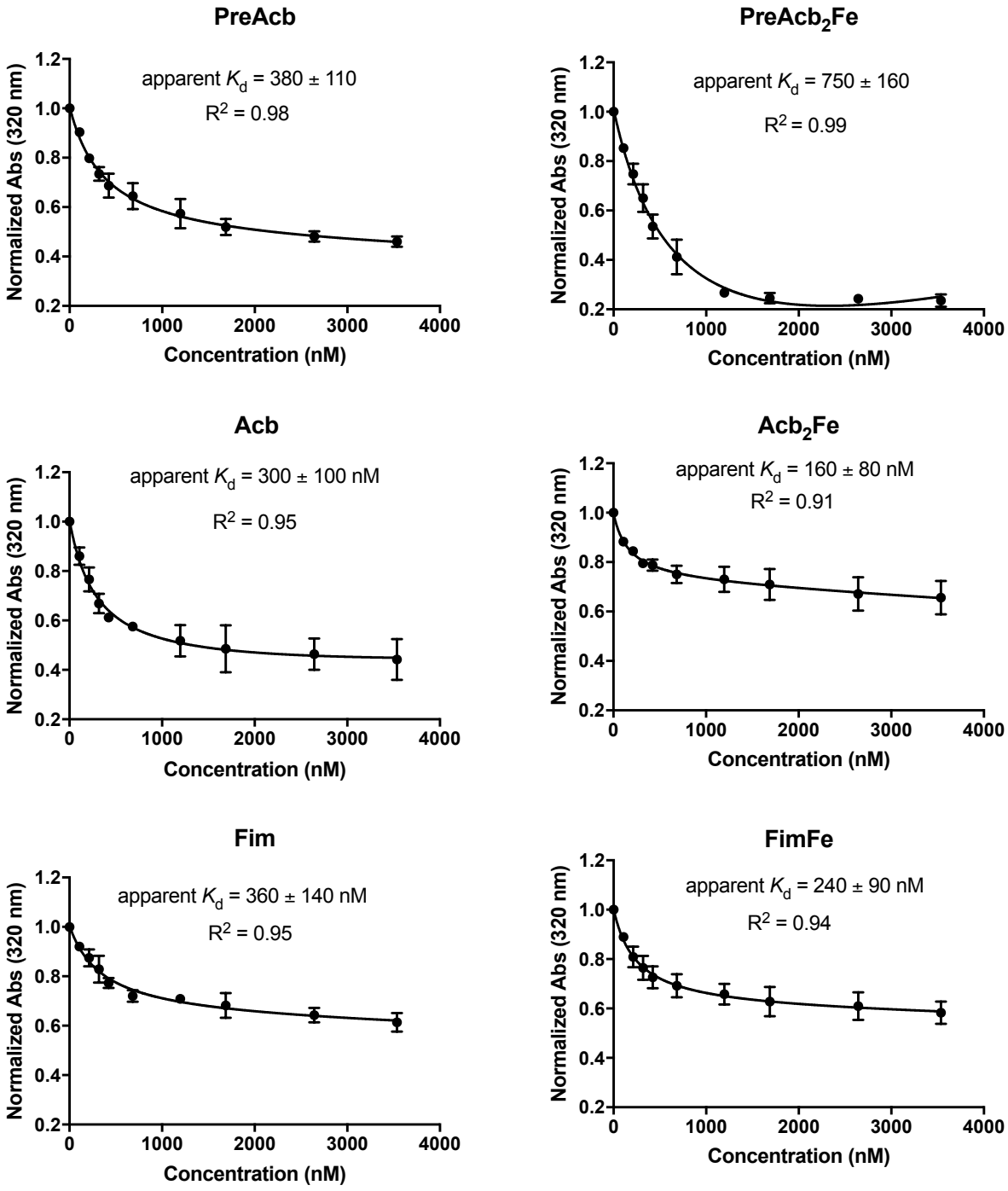

Supplementary Figure 22. Siderophore-dependent fluorescence quenching of *N*-His$_6$-BauB. Graphs depict intrinsic tryptophan fluorescence quenching (y-axis; $\lambda_{excitation}$ = 280 nm; $\lambda_{emission}$ = 320 nm) of 400 nM *N*-His$_6$-BauB in the presence of variable siderophore concentrations (x-axis). Apparent K_d values were calculated using a single-binding mode curve-fitting model in GraphPad Prism version 7.0b. Error bars represent standard deviations for two independent trials.

Acinetobactin BGCs

ATCC 19606 (GenBank: GCA_000162295.1)

ATCC 19606 (GenBank: GCA_002811175.1)

Acinetoferrin/Baumannoferrin BGCs

ATCC 19606 (GenBank: GCA_000162295.1)

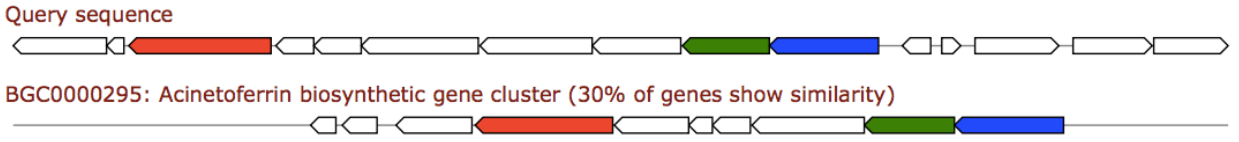

ATCC 19606 (GenBank: GCA_002811175.1)

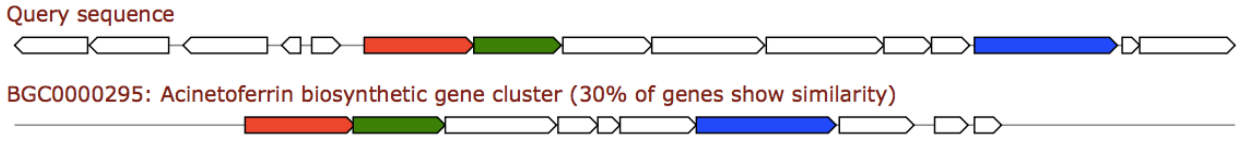

Supplementary Figure 23. Antismash analysis of two deposited genomes of *A. baumannii* ATCC 19606 turned up acinetobactin and acinetoferrin/baumannoferrin as the only siderophore BGCs present in the genome. No fimsbactin BGCs were detected.

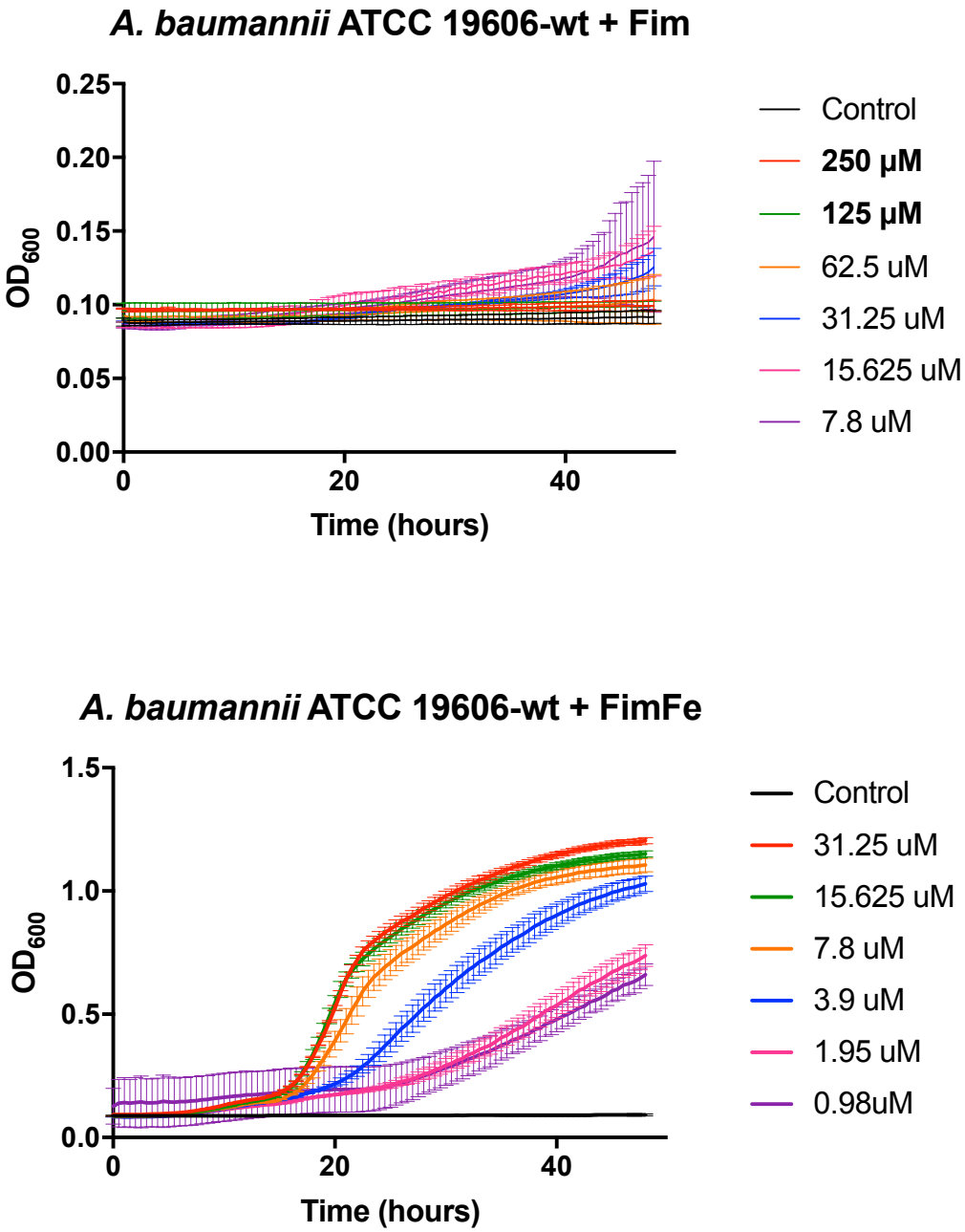

Supplementary Figure 24. Dose dependent influence of *apo*-Fim and *holo*-FimFe on *A. baumannii* ATCC 19606T growth. Line graphs depict the growth of wild-type *A. baumannii* ATCC 19606T in M9 minimal medium supplemented with 175 µM 2,2′-dipyridyl (DIP) determined by measuring the optical density at 600 nm (OD_{600}) at 37 °C as a function of time in the presence of variable siderophore concentrations. Error bars represent standard deviations from the mean for three independent trials.

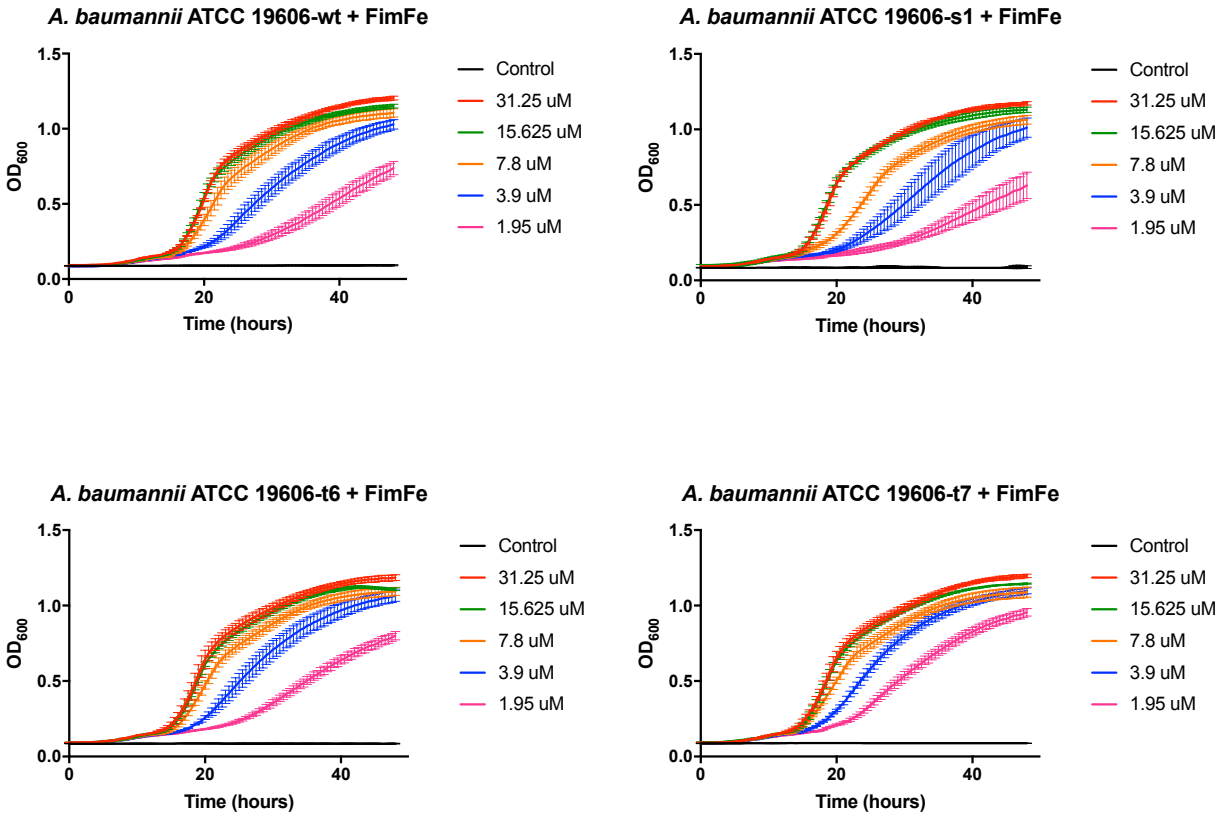

Supplementary Figure 25. Dose dependent growth promotion of *A. baumannii* ATCC 19606T strains by *holo*-FimFe. Line graphs depict the growth of wild-type (wt), s1-mutant (insertional mutant in *basD*, deficient in PreAcb/Acb biosynthesis), t6-mutant (insertional mutation in *bauA*, deficient in PreAcb/Acb import to periplasm), and t7-mutant (insertional mutation in *bauD*, deficient in PreAcb/Acb import to cytoplasm) strains of *A. baumannii* ATCC 19606 in M9 minimal medium supplemented with 175 μM 2,2′-dipyridyl (DIP) determined by measuring the optical density at 600 nm (OD_{600}) at 37 °C as a function of time in the presence of variable siderophore concentration. Error bars represent standard deviations from the mean for three independent trials.

***N*-His$_6$-BauB in pET28bTEV (cleavable *N*-term His-tag):**

Nucleotide:

AAGGAGATATACCATGGGCAGCAGCCATCATCATCATCATCACAGCAGCGGCGAAAACC
TGTATTTTCAG↓GGCCATATGTGCGACCAAAAAGTTGCGGATACCACCCAGGCGAGCCAAA
AACTGGCGGAGCCGATTACCGTTAAGCACGCGCTGGGCACCACCGTGATCGACCACCTGCC
GCAGCGTGTGGCGGTTCTGGATATGAACGAAGCGGACTTCCTGGATCAACTGAACGTTCCGA
TTATGGGCATGCCGAAAGACTACGTGCCGCACTTTCTGGAGAAGTATAAAAAGGACGCGCA
GATTCAAGATCTGGGTGCGATCGTTCAGCCGAACATGGAACGTATTTATGCGCTGAAACCGG
ATCTGATCCTGATGACCCCGCTGCACGTGAACCAGTACCAAGAGCTGAGCAAGATCGCGCC
GACCATTCACTATGACATCAACTTCAACAACAGCGAAAGCAACCACATTGGCCTGGTTAAAG
ATCACATGATGACCCTGGGTAAAATCTTTAACAAAGAGGACCTGGCGCGTCAGAAAGTGAG
CGAGCTGGATGAACAAGTGAAGCAGGTTCAAGCGGTGACCGCGAACCGTCCGGAACGTGCG
CTGGTTGTGCTGCACAACAACGGTGCGTTCAGCAACTTTGGCATTCAGAGCCGTTACGGTTT
CATCTTTAACGCGTTCGGCGTTAAGCCGGCGAGCGGTGTGGTTGACACCAGCCTGCACGGTC
AACCGATTAGCAGCGAGTTTATCAAAAAGGCGGACCCGGATATCCTGTATATTGTTGATCGT
ACCGCGGTGATGGAGCACCGTCCGAACATCAACGCGGCGAGCGTGGAAAACCCGCTGCTGC
GTCAGACCAAAGCGTGGAAGAACGGCCGTGTTATTTTCGTTGATGCGGATGCGTGGTACACC
ACCGCGGCGAGCCCGACCAGCCTGAAGATCGTTATGGAAGACGTGAAAAAGGGTTATCAAT
AAAAGCTT

Amino Acid:

GSSHHHHHHSSGENLYFQ↓GHMCDQKVADTTQASQKLAEPITVKHALGTTVIDHLPQRVA
VLDMNEADFLDQLNVPIMGMPKDYVPHFLEKYKKDAQIQDLGAIVQPNMERIYALKPDLI
LMTPLHVNQYQELSKIAPTIHYDINFNNSESNHIGLVKDHMMTLGKIFNKEDLARQKVSE
LDEQVKQVQAVTANRPERALVVLHNNGAFSNFGIQSRYGFIFNAFGVKPASGVVDTSLHG
QPISSEFIKKADPDILYIVDRTAVMEHRPNINAASVENPLLRQTKAWKNGRVIFVDADAW
YTTAASPTSLKIVMEDVKKGYQ

Supplementary Figure 26. Nucleotide and amino acid sequence of *N*-His$_6$-BauB in pET28bTEV (TEV-cleavable *N*-term hexahistidine-tag).[14] Start and stop codons are underlined. The TEV cleavage site is indicated by an arrow↓. The 969-bp *bauB* gene from *Acinetobacter baumannii* (Genbank Accession Number AAT52185) was used as the sequence template for subcloning.

II. Supplementary Tables

Supplemental Table 1. NMR characterization data for purified fimsbactin A from this work compared with previously reported data from the original isolation and characterization of fimsbactin A.[1]

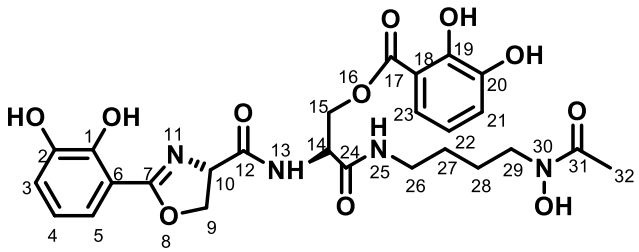

	^{13}C – Reported[1]	^{13}C - Observed	^{1}H – Reported[1]	^{1}H - Observed
1	148.2	148.2		
2	145.7	145.7		
3	119.3	119.5	6.968 (dd)	6.97 (dt)
4	118.6	118.7	6.74 (t)	6.74 (t)
5	117.7	117.9	7.08 (dd)	7.07 (dd)
6	110.1	110.1		
7	166.3	163.6		
9	69.1	69.3	4.52 (dd)	4.52 (dd)
			4.61 (dd)	4.60 (m)
10	66.9	67.2	5.06 (dd)	5.06 (dd)
11				
12	169.9	168.9		
13			8.72 (dd)	8.74 (d)
14	51.5	51.7	4.72 (m)	4.72 (m)
15	64.3	64.5	4.39 (m)	4.39 (dd)
			4.61 (m)	4.60 (m)
17	168.7	167.9		
18	112.8	112.8		
19	149.5	149.5		
20	146.0	146.0		
21	120.7	120.9	6.97 (dd)	6.97 (dt)
22	118.6	118.8	6.59 (t)	6.59 (t)
23	119.6	119.8	7.15 (dd)	7.15 (dd)
24	167.7	166.5		
25			8.23 (dt)	8.26 (t)
26	38.3	38.5	3.10 (m)	3.09 (m)
27	25.9	26.4	1.38 (m)	1.38 (m)
28	23.5	23.7	1.49 (m)	1.49 (m)
29	46.3	46.5	3.45 (t)	3.45 (t)
31	170.1	170.1		
32	20.1	20.3	1.96 (s)	1.96 (s)

Supplemental Table 2. Concentrations of test compounds used in combination for *A. baumannii* growth studies. For each combination of compounds 1 and 2, all possible concentrations were tested in duplicate as independent trials using a checkerboard arrangement in a 96-well plate.

Compound 1	Compound 2	[Compound 1] (μM)	[Compound 2] (μM)
Acb	Fim	3.9, 15.6, 62.5	3.9, 15.6, 62.5
[Fe(Acb)$_2$]	Fim	0.5, 3.9, 15.6	3.9, 15.6, 62.5
Acb	[Fe(Fim)]	3.9, 15.6, 62.5	0.5, 3.9, 15.6
Fim	[Fe(Fim)]	3.9, 15.6, 62.5	0.5, 3.9, 15.6

III. Supplementary Equations

As described in the experimental methods section of the main text, an EDTA competition experiment was used to measure the apparent K_{Fe} for FimFe at pH 7.4. The following equations were used to calculate apparent K_{Fe} based on the change in optical absorbance observed at 500 nm for FimFe in the presence of 1.2 equivalents of EDTA. A K_{Fe} value of $10^{25.1}$ was used for EDTA at pH 7.4 in final calculations.[15]

(1) $K_L = \frac{[\mathrm{FeL}]}{[Fe^{3+}][L]}$ for the following equilibrium; $[\mathrm{Fe^{3+}}] + [\mathrm{L}] \rightleftharpoons [\mathrm{FeL}]$

(2) $K_{FeEDTA} = \frac{[FeEDTA]}{[Fe^{3+}]\,[EDTA]}$ for the following equilibrium; $[\mathrm{Fe^{3+}}] + [\mathrm{EDTA}] \rightleftharpoons [\mathrm{FeEDTA}]$

(3) $K_{Exchange} = \frac{K_L}{K_{FeEDTA}}$ for the following equilibrium; $[\mathrm{FeEDTA}] + [\mathrm{L}] \rightleftharpoons [\mathrm{FeL}] + [\mathrm{EDTA}]$

(4) $K_{Exchange} = \frac{[FeL][EDTA]}{[FeEDTA][L]}$

(5) $\Delta = \frac{Abs_{FeL} - Abs_{FeL+EDTA}}{\varepsilon_L}$

(6) $K_L = K_{FeEDTA} \times \frac{[FeL][EDTA]}{[FeEDTA][L]}$

(7) $[FeL] = \frac{Abs_{FeL}}{\varepsilon_L}$

(8) $[EDTA] = [EDTA]_T - \Delta$ where $[\mathrm{EDTA}]_T$ = total EDTA added

(9) $[FeEDTA] = \Delta$

(10) $[L] = \Delta$

(11) K_{Fe} = apparent K_L

IV. Acknowledgements

The authors would like to thank J. Kao and M. Singh (WUSTL Chemistry) for help with the acquisition of 2D NMR data and B. Evans (Danforth Plant Science Center, St. Louis, MO) for help with the acquisition of HRMS data with support from NSF Award DBI-0521250. We thank L. Actis (Miami University) for providing the s1, t6, and t7 mutant strains of *A. baumannii* ATCC 19606T. The pET28bTEV plasmid encoding for *N*-His_6-BauB was provided by D. Bailey and A. Gulick, State University of New York at Buffalo. The research reported here was supported by NSF CAREER Award 1654611 to TAW.

V. References

1. Proschak, A.; Lubuta, P.; Grün; Löhr, F.; Wilharm, G.; De Berardinis, V.; Bode, H. B. "Structure and biosynthesis of fimsbactin A–F, siderophores from *Acinetobacter baumannii* and *Acinetobacter baylyi*." *ChemBioChem* **2013**, *14*, 633–638.

2. Dorsey, C. W.; Tomaras, A. P.; Connerly, P. L.; Tolmasky, M. E.; Crosa, J. H.; Actis, L. A. "The siderophore-mediated iron acquisition systems of *Acinetobacter baumannii* ATCC 19606 and *Vibrio anguillarum* 775 are structurally and functionally related." *Microbiology* **2004**, *150*, 3657–3667.

3. Penwell, W. F.; DeGrace, N.; Tentarelli, S.; Gauthier, L.; Gilbert, C. M.; Arivett, B. A.; Miller, A. A.; Durand-Reville, T. F.; Joubran, C.; Actis, L. A. "Discovery and characterization of new hydroxamate siderophores, baumannoferrin A and B, produced by *Acinetobacter baumannii*." *ChemBioChem* **2015**, *16*, 1896–1904.

4. Blin, K.; Wolf, T.; Chevrette, M. G.; Lu, X.; Schwalen, C. J.; Kautsar, S. A.; Suarez Durn, H. G.; de los Santos, E. L. C.; Uk Kim, H.; Nave, M.; Dickschat, J. S.; Mitchell, D. A.; Shelest, E.; Breitling, R.; Takano, E.; Yup Lee, S.; Weber, T.; Medema, M. H. "antiSMASH 4.0–improvements in chemistry prediction and gene cluster boundary identification." *Nucleic Acids Research* **2017**, *45*, W36–W41.

5. Funahashi, T.; Tanabe, T.; Maki, J.; Miyamoto, K.; Tsujibo, H.; Yamamoto, S. "Identification and characterization of a cluster of genes involved in biosynthesis and transport of acinetoferrin, a siderophore produced by *Acinetobacter haemolyticus* ATCC 17906." *Microbiology* **2013**, *159*, 678–690.

6. Carrano, C. J.; Jordan, M.; Dreschsel, H.; Schmid, D. G.; Winkelmann, G. "Heterobactins: A new class of siderophores from *Rhodococcus erythropolis* IGTS8 containing both hydroxamate and catecholate donor groups." *Biometals* **2001**, *14*, 119–125.

7. Mukai, A.; Komaki, H.; Takagi, M.; Shin-ya, K. "Novel siderophore, JBIR-16, isolated from *Nocardia tenerifensis* NBRC 101015." *The Journal of Antibiotics* **2009**, *62*, 601–603.

8. Griffiths, G. L.; Sigel, S. P.; Payne, S. M.; Neilands, J. B. "Vibriobactin, a siderophore from *Vibrio cholera*." *Journal of Biological Chemistry* **1984**, *259*, 383–385.

9. Okujo, N.; Saito, M.; Yamamoto, S.; Yoshida, T.; Miyoshi, S.; Shinoda, S. "Structure of vulnibactin, a new polyamine-containing siderophore from *Vibrio vulnificus*." *Biometals* **1994**, *7*, 109–116.

10. Yamamoto, S.; Okujo, N.; Fujita, Y.; Saito, M.; Yoshida, T.; Shinoda, S. "Structures of two polyamine-containing catecholate siderophores from *Vibrio fluvialis*." *J. Biochem.* **1993**, *113*, 538–544.

11. Ong, S. A.; Peterson, O. T.; Neilands, J. B. "Agrobactin, a siderophore from *Agrobacterium tumefaciens*." *Journal of Biological Chemistry* **1979**, *254*, 1860–1865.

12. (a) Tait, G. H. "The identification and biosynthesis of siderochromes formed by *Micrococcus denitrificans*." *Biochem. J.* **1975**, *146*, 191–204; (b) Peterson, T.; Neilands, J. B. "Revised structure of a catecholamide spermidine siderophore from *Paracoccus denitrificans*." *Tetrahedron Letters* **1979**, *50*, 4805–4808.

13. Cornish, A. S.; Page, W. J. "Production of the triacetecholate siderophore protochelin by *Azotobacter vinelandii*." *Biometals* **1995**, *8*, 332–338.

14. Bailey, D. C.; Bohac, T. J.; Shapiro, J. A.; Giblin, D. E.; Wencewicz, T. A.; Gulick, A. M. "Crystal structure of the siderophore binding protein BauB bound to an unusual 2:1 complex between acinetobactin and ferric iron." *Biochemistry* **2018**, *57*, 6653–6661.

15. Martell, A. E., and Smith, R. M. (1974) Critical stability constants, Vol. 1, Plenum Press, New York, NY.